Journal of Applied Physics

RESEARCH ARTICLE | MAY 01 2024

Thermoelectric properties and thermal transport in two-dimensional $GaInSe_3$ and $GaInTe_3$ monolayers: A first-principles study

Special Collection: Thermal Transport in 2D Materials

Himanshu Nautiyal ; Paolo Scardi

J. Appl. Phys. 135, 174301 (2024)
https://doi.org/10.1063/5.0207618

AIP Publishing

Journal of Applied Physics ARTICLE pubs.aip.org/aip/jap

Thermoelectric properties and thermal transport in two-dimensional $GaInSe_3$ and $GaInTe_3$ monolayers: A first-principles study

Cite as: J. Appl. Phys. **135**, 174301 (2024); doi: 10.1063/5.0207618
Submitted: 9 March 2024 · Accepted: 18 April 2024 ·
Published Online: 1 May 2024

Himanshu Nautiyal[a] and Paolo Scardi[a]

AFFILIATIONS

Department of Civil, Environmental & Mechanical Engineering, University of Trento, via Mesiano 77, Trento 38123, Italy

Note: This paper is part of the special topic, Thermal Transport in 2D Materials.
[a]**Authors to whom correspondence should be addressed:** himanshu.nautiyal@unitn.it and paolo.scardi@unitn.it

ABSTRACT

We here report the electronic structure calculation of $GaInSe_3$ and $GaInTe_3$ monolayers with the P3m1 (no. 156) space group. The electronic structure and thermoelectric properties of the monolayers are calculated through the Vienna *Ab initio* Simulation Package and BoltzTraP2 codes. The dynamic and thermodynamic stabilities were verified by calculating their phonon spectra and simulating *ab initio* molecular dynamics. The monolayers were found to have a direct bandgap, with both PBE + SOC and HSE06 + SOC potentials. The lattice thermal conductivity of $GaInTe_3$ monolayer calculated using Phono3py code shows ultra-low values due to enhanced phonon–phonon scattering. Combining electrical and thermal transport, the values have been evaluated. Importantly, the p-type $GaInTe_3$ has excellent thermoelectric properties at 700 K, with a zT value of 2, indicating that the p-type $GaInTe_3$ has potential application in the field of thermoelectricity.

I. INTRODUCTION

To fulfill the demand of green energy, electricity can be reproduced from waste heat through thermoelectric effects. Thermoelectric materials convert temperature gradients into electrical potentials and are of widespread interest for their applications in solid-state power generation or refrigeration.[1] The devices used for harvesting the thermal energy and transform it to electrical are called thermoelectric generators (TEGs). Materials with a high thermoelectric figure of merit (zT) are of great importance to be employed in high efficiency,

$$zT = \frac{S^2\sigma}{\kappa}T,$$

where T is the absolute temperature, σ is the electrical conductivity, S is the Seebeck coefficient, and κ is the thermal conductivity composed of two parts lattice thermal conductivity (κ_L) and electronic thermal conductivity (κ_E).

Interdependency among these parameters poses a challenge in designing excellent thermoelectric materials with high zT. For real device applications, several approaches have been applied to achieve high zT; structural modification leading to an enhancement of power factor by the band engineering, carrier doping, alloying, as well as the reduction of the lattice thermal conductivity through efficient phonon scattering materials. Critical considerations for thermoelectric materials include the requirement of low thermal conductivity, which typically means soft, anharmonic bonding or unusual phonon behavior. Conversely, achieving high power factor requires favorable electrical properties, such as high conductivity and thermopower. This typically entails special band structure features, such as multiple carrier pockets, carrier pocket anisotropy, and non-parabolicity.[2,3]

Among many candidates, bulk type PbTe[4] and Bi_2Te_3[5] are the most well-known TE materials because they display rather high $zT = 1$–2. However, this high performance is observed at high temperatures (>600 K), and the high zT value is rapidly decreased if the temperature or carrier concentration deviates from the optimum condition. Thus, the high zT is preserved only in limited conditions. This limitation poses significant obstacle for practical device applications.

2D materials have properties that are distinct from three-dimensional (3D) materials. Recently, it has been proposed that the Seebeck coefficient in two-dimensional (2D) material can be significantly enhanced due to the quantum confinement effect.[6,7] Hicks and Dresselhaus proposed that reducing dimensionality and harnessing the effects of quantum confinement on electronic transport could substantially improve the power factor of materials. Since the discovery of graphene,[8,9] increasing numbers of two-dimensional (2D) materials have been investigated.

Numerous 2D layered structures beyond graphene have been extensively studied.[10] Notable examples of successfully synthesized 2D materials include graphene,[8,9] silicene,[11] germanene,[12] phosphorene,[13] transition metal dichalcogenides (TMDs),[14–18] and monochalcogenides.[19,20] These materials exhibit promising characteristics for a wide array of applications spanning electronics,[21] optoelectronics,[22] thermoelectricity,[23] gas sensing,[24] water splitting,[25] ferroelectricity,[26] and piezoelectricity.[26] The versatile properties of 2D materials suggest immense potential for advancements in various technological domains.

Recent studies have unveiled the remarkably low lattice thermal conductivity exhibited by 2D materials and have emerged as promising candidates for thermoelectric applications. The prediction of Janus monolayers such as In_2SSe,[27] MoSSe,[28] WS-Se/Te,[29,30] SnSSe[31,32] has paved the way for exploration into these newly envisaged materials. The Janus In_2XY (X/Y = S, Se, Te) monolayers are found to be potential candidates for thermoelectric, optoelectronic, and photocatalytic applications.[33] Recently, the In_2Se_3 monolayer has been successfully synthesized by Almeida *et al.*[34] Furthermore, the Janus Ga_2XY (X, Y = S, Se, Te) monolayers are promising candidates for ultraviolet piezoelectric, photodetector, and thermoelectric applications.[35,36] Additionally, GaX (X = S, Se, Te) monolayers have also emerged as suitable candidates for low temperature thermoelectric applications.[37] Vu *et al.*[38] have studied the $GaInX_3$ (X = S, Se, Te) monolayers using first principle calculations for structural, electronic, and work functions relevant to photocatalytic applications. They have utilized the DFT-D2 method without incorporating the effect of spin–orbit coupling. However, to the best of our knowledge, no studies have been done to investigate the temperature-dependent thermoelectric properties and thermal transport of $GaInSe_3$ and $GaInTe_3$ monolayers. Therefore, to address this gap and identify a promising candidate capable of converting waste heat into useful electrical energy for thermoelectric applications, we have investigated the thermoelectric properties and thermal transport of $GaInSe_3$ and $GaInTe_3$ monolayers in detail by using the density functional theory (DFT).

In this work, we conduct comprehensive investigation of electrical and phonon transport properties of monolayer $GaInSe_3$ and $GaInTe_3$ using first principle density functional theory (DFT) calculations. Our analysis includes determination of band structures, phonon dispersion curves, the Seebeck coefficient, electrical and thermal conductivity, relaxation time, and thermoelectric figure of merit. Through *ab initio* molecular dynamics (AIMD) and phonon dispersion calculations, we confirm the thermal and dynamical stability of the monolayers. Our research findings suggest that the investigated monolayers hold significant potential for thermoelectric applications.

II. COMPUTATIONAL METHOD

A. DFT

The Vienna *Ab initio* Simulation Package (VASP)[39,40] employed the projector augmented wave (PAW) method to conduct geometry optimization. Energy convergence was achieved through the GGA-PBE functional,[41] incorporating van der Waals interactions via the semi-empirical DFT-D3 correction.[42] Monolayers were modeled with a 20 Å vacuum spacing between periodic layers along the z-direction to avoid interactions between adjacent monolayers. Employing a plane wave basis set, a cutoff energy of 400 eV was used with an $11 \times 11 \times 1$ Monkhorst–Pack k-mesh.[43] During relaxation, the cell shape was permitted to change while preserving a constant cell volume. To achieve convergence in the electronic self-consistent field iterations, a threshold of 10^{-6} eV was set. Atom positions were optimized until the maximum Hellman–Feynman force on each atom dropped below 0.0001 eV $Å^{-1}$. Because of the heavy atomic mass of atoms, the relativistic effects were taken into account by incorporating spin−orbit coupling (SOC). To ensure a comprehensive sampling of the Brillouin zone, a denser k-mesh of $41 \times 41 \times 1$ was employed, utilizing the tetrahedron method with Blöchl corrections.

B. *Ab initio* molecular dynamics (AIMD)

The thermal stability of materials is a critical property to guarantee that they can be used in practical applications. *Ab initio* molecular dynamics (AIMD) simulations were performed within a canonical (NVT) ensemble, utilizing a Nosé–Hoover thermostat to maintain temperatures set at 300 and 700 K. The simulation model employed a supercell consisting of $4 \times 4 \times 1$ unit cells. Throughout the simulation, the system evolved with a time step of 2 femtoseconds over 10 000 steps, leading to a cumulative simulation time of 20 ps.

C. Phonon and lattice thermal conductivity

The harmonic second-order force constants (2nd IFCs) and phonon spectrum were computed utilizing Phonopy package,[44] employing a $4 \times 4 \times 1$ supercell, and a $3 \times 3 \times 1$ k-mesh. Subsequently, the phonon transport properties were assessed using Phono3py,[45] solving the phonon Boltzmann transport equation within the framework of the Single-Mode Relaxation Time Approximation (SMRTA). The anharmonic third-order interaction force constants (3rd IFCs) were derived through the finite-difference method, utilizing a $3 \times 3 \times 1$ supercell and a $3 \times 3 \times 1$ k-mesh. Furthermore, a meticulous evaluation of the convergence of the κ_L with respect to the q-mesh was conducted. A dense $41 \times 41 \times 1$ k-mesh was employed specifically for computing the lattice thermal conductivity.

D. Transport property

The Seebeck coefficient (S) and electrical conductivity over the relaxation time (σ/τ) are obtained through the BoltzTraP2[46] with the Constant Relaxation Time Approximation (CRTA). The Bardeen−Shockley deformation potential (DP) theory[47] was used to calculate the relaxation time.

III. RESULTS AND DISCUSSION

The studied 2D monolayers have a hexagonal structure with a space group P3m1 (no. 156). The structures of the relaxed monolayers are shown in Fig. 1. The structural information of the relaxed monolayers is reported in Table I. After optimization, the in-plane lattice constants of $GaInSe_3$ and $GaInTe_3$ monolayers were 3.955 and 4.264 Å, respectively, whereas the layer thicknesses along the z-direction are 6.538 and 7.122 Å, respectively. The obtained lattice parameters are in good agreement with the results in the available literature.[38] It was observed that the In–X and Ga–X bonds increase as the X atom varies from Se to Te, which is strongly connected with the atomic radius of the X element.

The cohesive energy E_C of the monolayers can be evaluated by

$$E_C = \frac{N_{Ga}E^{Iso}_{Ga} + N_{In}E^{Iso}_{In} + N_X E^{Iso}_X - E_{GaInX_3}}{N_{Ga} + N_{In} + N_X}.$$

Here, N_{Ga}, N_{In}, and N_X are the number of Ga, In, and X = Se, Te atoms in the simulated monolayers. While E^{Iso}_{Ga}, E^{Iso}_{In}, and E^{Iso}_X are the energy of the respective isolated atom, and finally, E_{GaInX_3} is the energy of the respective monolayer system.

The cohesive energy of $GaInSe_3$ and $GaInTe_3$ was found to be 3.85 and 3.39 eV, respectively, and both simulated structures are turned out to be energetically favorable.

The thermal stability of materials is a crucial property to ensure that they can be used in practical applications. In this work, the thermal properties of $GaInSe_3$ and $GaInTe_3$ are investigated by AIMD simulations at 300 and 700 K for 20 ps (10 000 time steps). Snapshots of the atomic structure before and after heating and the time-dependent temperature fluctuation of $GaInSe_3$ and $GaInTe_3$ by AIMD simulations are also shown in Fig. 2. Figure S1 in the supplementary material shows the variation of energy with time, where the energy fluctuates with the simulation time around the average energy value. The obtained results confirm that the $GaInSe_3$ and $GaInTe_3$ monolayers exhibit high thermal stability. Furthermore, neither bond breakage nor structural reconstruction occurs in the $GaInSe_3$ and $GaInTe_3$ monolayers.

The elastic constants C_{ij} give important information about the stability and stiffness of materials. They were determined by computing the stress generated by applying a small strain to an optimized unit cell. The elastic tensor coefficients are calculated and are listed in Table II. It was clear that the monolayer was mechanically stable since they satisfy the stability criteria $C_{11} > 0$ and

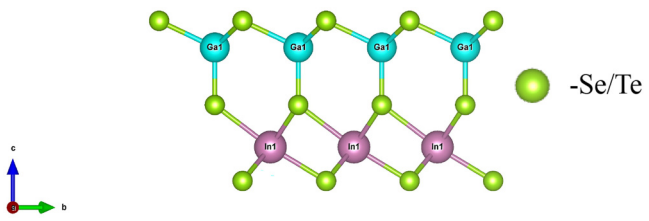

FIG. 1. Crystal structure of $GaInSe_3$ and $GaInTe_3$ monolayers. The atomic structure is produced using VESTA software.[48]

TABLE I. The structure parameter and cohesive energy of the $GaInSe_3$ and $GaInTe_3$ monolayers.

Properties	$GaInSe_3$	$GaInTe_3$
Lattice parameter	a = b = 3.955 Å a = b = 3.90 Å (DFT-D2)[38]	a = b = 4.264 Å a = b = 4.19 Å (DFT-D2)[38]
Lattice angle	$\alpha = \beta = 90°,\ \gamma = 120°$	$\alpha = \beta = 90°,\ \gamma = 120°$
Thickness	6.538 Å	7.122 Å
Bond lengths	Ga-Se1 = 2.347 59 Å Ga-Se2 = 2.529 49 Å In-Se1 = 2.858 82 Å In-Se3 = 2.668 71 Å	Ga-Te1 = 2.568 18 Å Ga-Te2 = 2.739 75 Å In-Te1 = 3.065 57 Å In-Te3 = 2.895 42 Å
Cohesive energy	3.85 eV	3.39 eV

$C_{11} > |C_{12}|$.[49] Then, the transverse and longitudinal sound velocity can be analyzed by shear modulus (G) and bulk modulus (B) with the formula[50,51]

$$v_T = \sqrt{\frac{G}{\rho}} \quad \text{and} \quad v_L = \sqrt{\frac{\left(B + \frac{3}{4}G\right)}{\rho}},$$

where ρ is the density. We use density values of 4.47×10^{-3} and 5.18×10^{-3} g/m^2 for layered $GaInSe_3$ and $GaInTe_3$.The average sound velocity v_m can be calculated by

$$v_m = \left[\frac{1}{3}\left[\frac{2}{v_t^3} + \frac{1}{v_L^3}\right]\right]^{-1/3}.$$

The Debye temperature θ_D can be obtained from average sound velocity by the formula[51]

$$\theta_D = \frac{\hbar v_m}{k_B}\left(\frac{4\pi N}{A}\right)^{1/2},$$

where $\hbar$ is the reduced Planck constant, k_B is the Boltzmann constant, N is the number of atoms in the unit cell, and A is the area of the unit cell.

The Grüneisen parameter γ reflects the anharmonicity in bonding, which is related to the strength of phonon scattering. From the estimation of elastic mechanical properties above, such as elastic constants, we can obtain the value of γ by the Poisson ratio $\nu\left(=\frac{C_{12}}{C_{11}}\right)$ with the formula

$$\gamma = \frac{3(1+\nu)}{2(2-\nu)}.$$

From the calculations, γ values are 1.202 and 1.1281 for $GaInSe_3$ and $GaInTe_3$, respectively. It is also noted that γ are smaller than the typical TE materials PbTe (1.96)[52] and SnSe (1.65).[53]

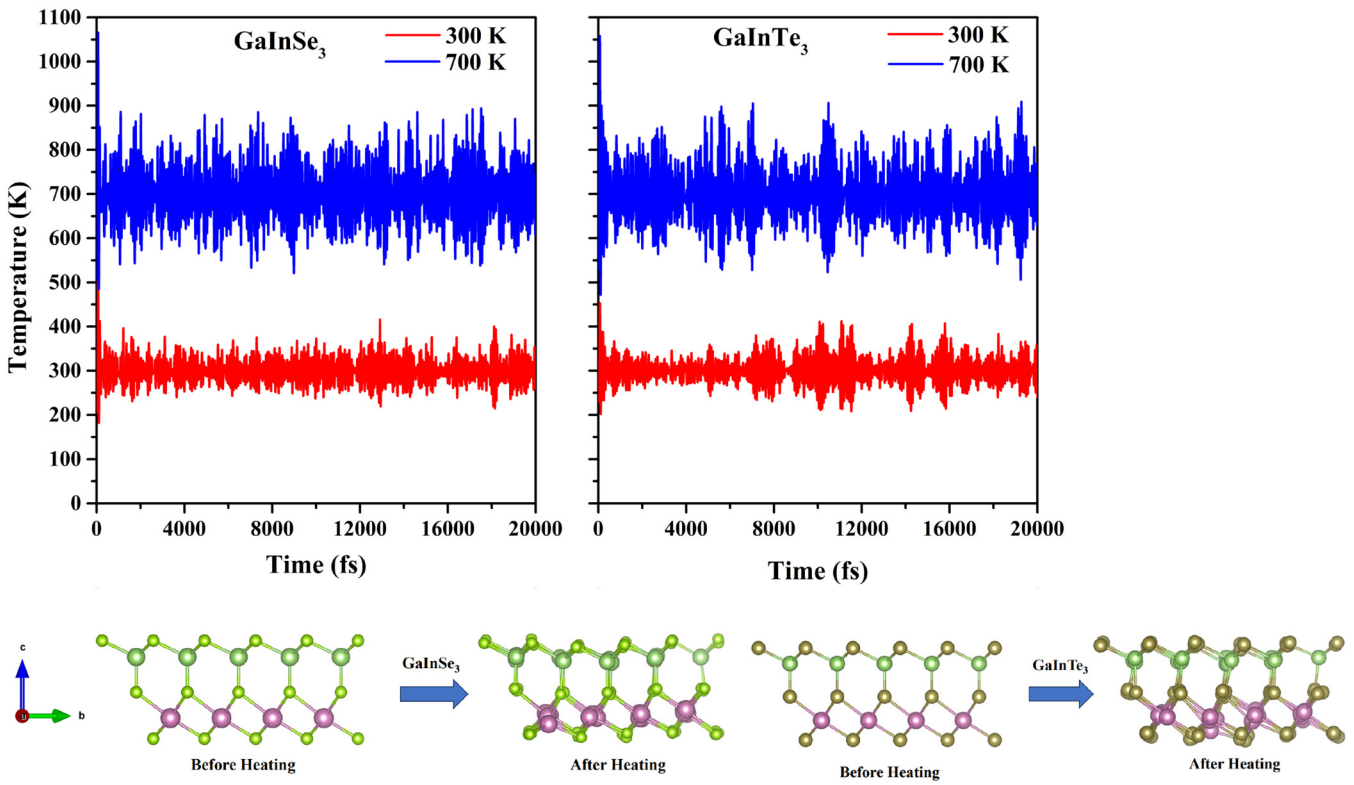

FIG. 2. Time-dependent AIMD simulations of temperature fluctuation as a function of time at 300 and 700 K. The images represent snapshots of monolayer structures before and after heating for 20 ps.

To study the dynamical stability of the monolayers, the phonon dispersion curve was calculated. Figure 3 displays the phonon dispersion along high-symmetry path. The long range Coulomb interaction gives rise to longitudinal/transverse optical splitting referred to as LO–TO splitting at the BZ center. The LO–TO splitting is addressed by incorporating the non-analytical term correction by calculating the Born effective charge (shown in Table III). The absence of the imaginary frequency mode in phonon spectra indicates that the simulated monolayers are dynamically stable. As the investigated structures contained five atoms in the primitive unit cell, the phonon dispersion curves exhibit 15 phonon branches, of which three are acoustic and the remaining are optical. The highest frequency of vibration in $GaInSe_3$ and $GaInTe_3$ was around 9 and 7.5 THz, respectively.

TABLE II. The elastic constants, Young's modulus, bulk modulus, Poisson's ratio, transverse and longitudinal sound velocity, Debye temperature, and Grüneisen parameter for monolayer $GaInSe_3$ and $GaInTe_3$.

Properties	$GaInSe_3$	$GaInTe_3$
C_{11} (N/m)	79.55	62.89
C_{12} (N/m)	26.61	24.04
C_{66}/shear modulus (N/m)	26.470	19.43
Young's modulus (N/m)	70.650	53.70
Bulk modulus (N/m)	53.08	43.47
Poisson's ratio (ν)	0.33	0.38
v_L (m/s)	4039.38	3347.28
v_T (m/s)	2433.45	1936.59
v_m (m/s)	2690.91	2149.58
θ_D (K)	411.83	305.14
γ	1.20	1.28
Mechanical stability	Stable	Stable

Figure 3 also illustrates the vibrational density of states (VDOSs) for both $GaInSe_3$ and $GaInTe_3$ monolayers. In the $GaInSe_3$ monolayer, the low-frequency modes (<2 THz) primarily stem from vibrations involving Ga and Se atoms, with Ga contributing more significantly. Conversely, higher frequency modes (>7 THz) are dominated by vibrations of In and Se atoms. On the other hand, in the $GaInTe_3$ monolayer, low-frequency modes (<2 THz) are predominantly associated with Ga and Te atoms, with Te exhibiting a higher contribution, while the high frequency modes (>6 THz) involve vibrations of In and Te atoms. A notable observation from the VDOS of $GaInTe_3$ is the higher dominance of Te atom vibrations in the frequency band from 1–5 THz compared to the Se atom in $GaInSe_3$ within the frequency band of 2–6 THz. This variation is attributed to the substantial mass difference between Se and

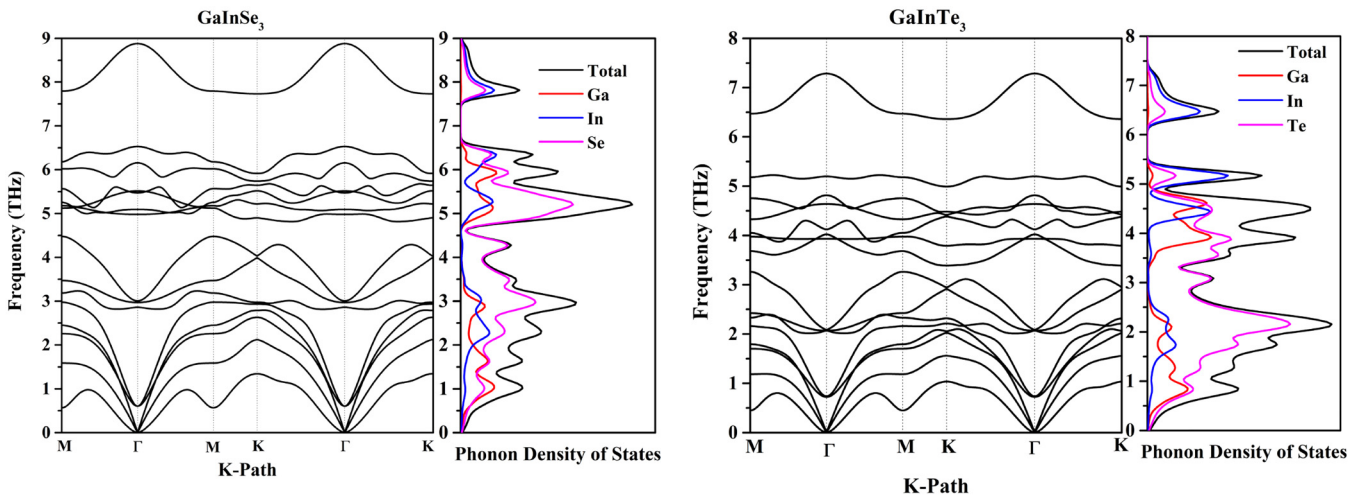

FIG. 3. Phonon dispersions curve and phonon density of states of the $GaInSe_3$ and $GaInTe_3$ monolayers.

Te atoms. These low-lying optical modes notably scatter the acoustic phonons, consequently resulting in a substantial reduction in lattice thermal conductivity, even below room temperature.

Group velocities of phonons have a significant influence on thermal transport, and they are obtained from the slope of the phonon dispersion curve

$$v_g = \nabla_k \omega(k),$$

where v_g is the group velocity, ω is the wave's angular frequency, k is the wave vector, and $\omega(k)$ is the frequency. A lower frequency and lower group velocity lead to lower lattice thermal conductivity. The group velocities are shown in Fig. 4. The group velocity of the optical branches is generally lower than the acoustic branches. The maximum group velocity for acoustic branches in $GaInSe_3$ and $GaInTe_3$ monolayers is around 4000 and 3500 m/s, respectively, in good agreement with the speed of sound calculated from the mechanical properties reported in Table II.

The lattice thermal conductivity (κ_L) is an important parameter to calculate the thermoelectric performance of materials. Based on the 2nd and 3rd IFCs, the κ_L of the monolayers can be calculated by solving the phonon Boltzmann transport equation.[45] The plot of lattice thermal conductivity with temperature is shown in Fig. 5. The κ_L is related to the velocity and lifetime of phonons and specific heat contribution of phonon $\left(\kappa_L = \frac{1}{3} C_V v_g^2 \tau_{ph}\right)$. As expected, κ_L decreases with the increase of temperature, which can be explained by the enhancement of intrinsic phonon–phonon scattering with increasing temperature. The κ_L of $GaInTe_3$ is lower than that of $GaInSe_3$. At 300 K, the lattice thermal conductivity of $GaInSe_3$ and $GaInTe_3$ is 2.25 and 0.65 $W\,m^{-1}\,K^{-1}$, respectively. The κ_L decrease to 1 and 0.3 $Wm^{-1}K^{-1}$ at 700 K for the two compounds, respectively.

TABLE III. Bader charge and Born effective charge tensor of the two monolayers.

Compound	Atom	Bader charge (e)	Born effective charge tensor (Z*)		
			Z_{XX}	Z_{YY}	Z_{ZZ}
$GaInSe_3$	Ga	0.637 145	3.915 56	3.915 56	0.398 47
	In	0.561 974	2.717 07	2.717 07	0.403 75
	Se1	−0.377 971	−1.592 17	−1.592 17	−0.410 66
	Se2	−0.401 1	−2.613 61	−2.613 61	−0.194 75
	Se3	−0.420 048	−2.426 86	−2.426 86	−0.196 81
$GaInTe_3$	Ga	0.220 942	4.242 30	4.242 30	0.321 50
	In	0.088 521	2.613 64	2.613 64	0.310 93
	Te1	−0.165 370	−1.591 02	−1.591 02	−0.313 43
	Te2	−0.016 095	−2.752 23	−2.752 23	−0.156 71
	Te3	−0.127 998	−2.512 70	−2.512 70	−0.162 29

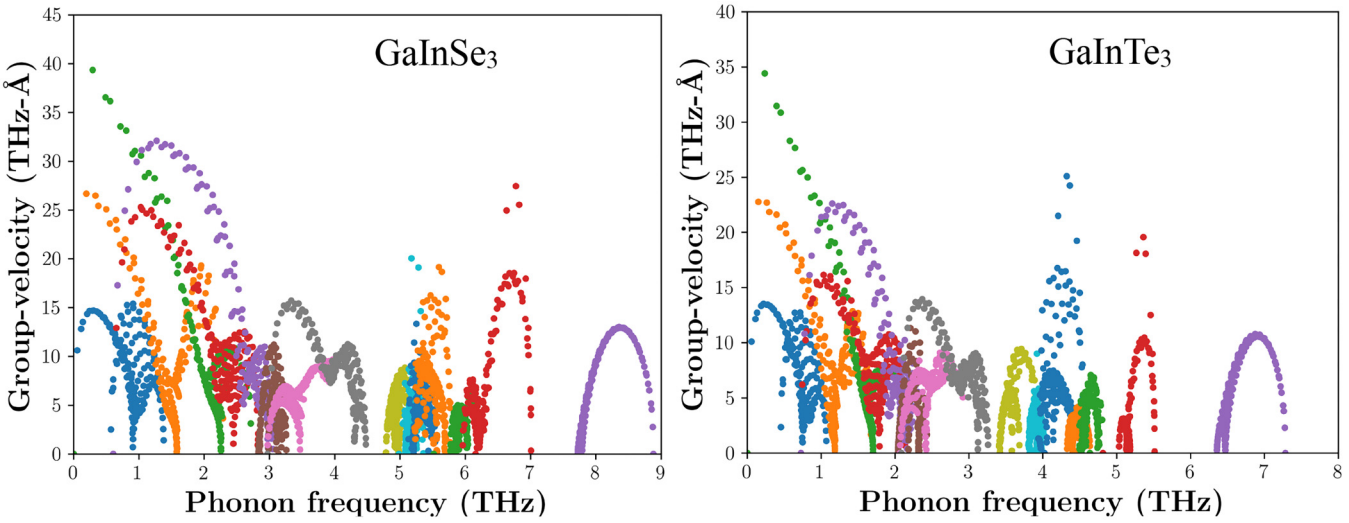

FIG. 4. Calculated phonon group velocities of the $GaInSe_3$ (left) and $GaInTe_3$ (right) monolayers. The blue, orange, and green colors represent the group velocity of the two transverse acoustic branches and one longitudinal acoustic branch, respectively. The rest are the group velocity of optical branches. From the figure, it can be observed that the violet color optical phonons in the case of $GaInSe_3$ have a higher group velocity of 33 THz Å, while in the case of $GaInTe_3$, it is around 24 THz Å.

The decrease in thermal conductivity with rising temperature is attributed to the softening of phonons. The lattice thermal conductivity depends on the slope of the acoustic phonon branches (i.e., the group velocity) and low-lying optical phonon branches in the phonon dispersion curve.[54] When the low-lying optical modes are present in a compound, the lattice thermal conductivity decreases as temperature rises, owing to phonon–phonon interactions, specifically Umklapp scattering. Typically, heat in a material is primarily transported by the acoustic branch, given the lower group velocity of optical phonon branches and their higher-frequency vibrations. When low-lying optical modes with significant group velocity occur, their contribution also becomes important at higher temperatures. These low group velocity optical phonons scatter the acoustic modes and the scattering rate increases, which decreases the lifetime of the phonons and, thus, the lattice thermal conductivity. As seen from the group velocity shown in Fig. 4, the group velocity of optical phonons in $GaInTe_3$ is much lower as compared to $GaInSe_3$. From the plot of phonon lifetime [Fig. 6], it is clearly visible that the lifetime of phonons in the $GaInSe_3$ monolayer (4 ps) is almost half that of $GaInTe_3$ (1.75 ps). The dramatic decrease in the phonon lifetime of $GaInTe_3$ is a consequence of the flatter low-lying optical modes.

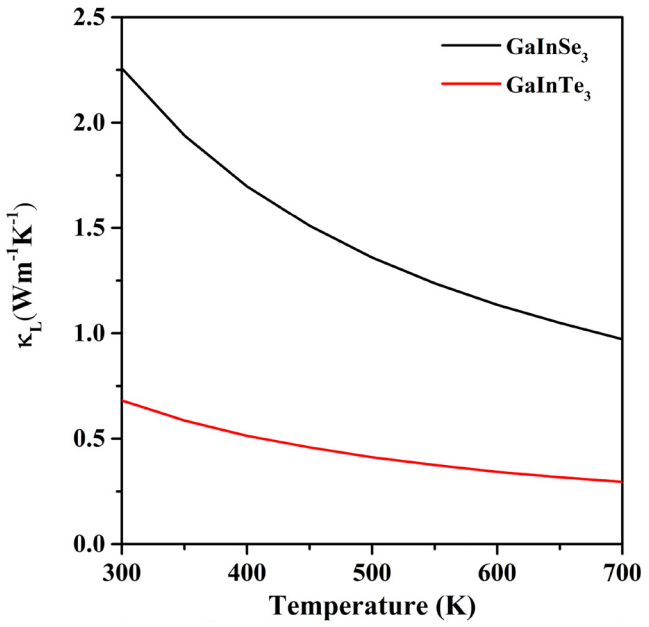

FIG. 5. Calculated lattice thermal conductivities of the $GaInSe_3$ and $GaInTe_3$ monolayers using SMRTA as implemented in the Phono3py code.

The Bader charge calculations were conducted to understand the essential bonding characteristics of the two structures. The results are summarized in Table III. For $GaInSe_3$ and $GaInTe_3$, the Bader charges for Ga and In are positive, indicating that these atoms have gained a significant positive charge, due to electron donation to Se atoms. Consequently, the Bader charges for Se/Te atoms are negative as they have gained electrons. However, in $GaInTe_3$, the Bader charges for Te atoms are slightly lower than those for Se in $GaInSe_3$. The presence of slightly lower Bader charges on Te atoms suggests a lesser degree of electron donation compared to the $GaInSe_3$ monolayer.

The results are confirmed by calculating the electron localization function (ELF) plot shown in Fig. 7. Electrons are localized in the case of $GaInSe_3$ for the central Ga–Se bond, while for Ga–Te,

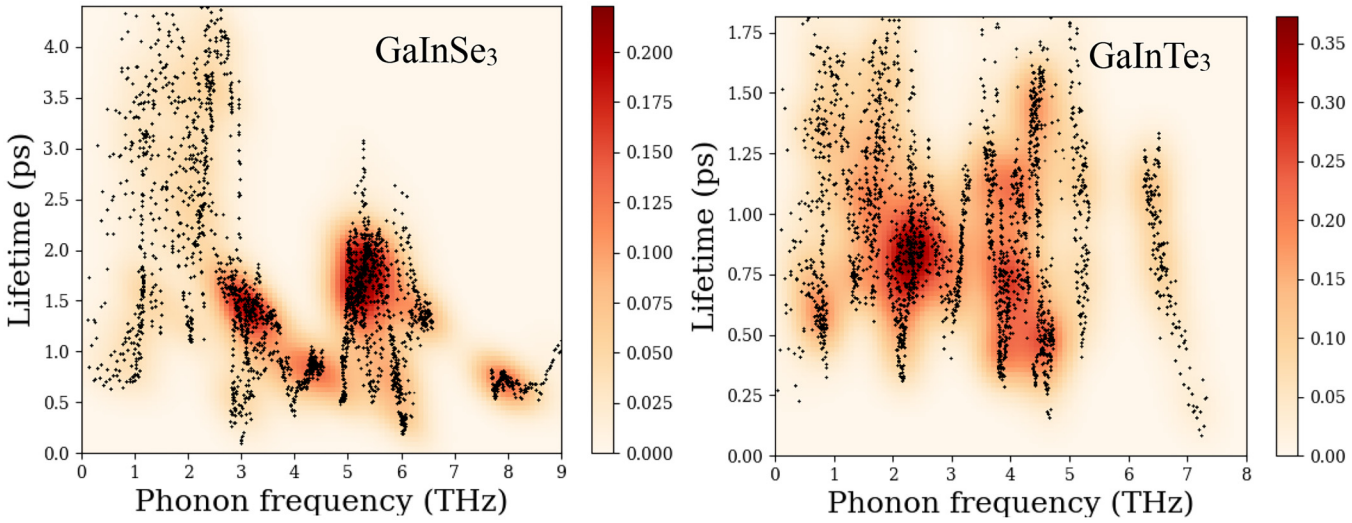

FIG. 6. Phonon lifetimes of the $GaInSe_3$ (left) and $GaInTe_3$ (right) monolayers calculated at 300 K. The color in the figure represents the phonon density. Bright color represents the higher phonon density.

they are delocalized, causing significant variation in bonding. The lower Bader charge on Te atoms in $GaInTe_3$ also shows that Te atoms are loosely bonded, which leads to a significant variation in bonding in the $GaInTe_3$ monolayer and causes domination of Te atom vibrations in the frequency range of 1.5–4 THz.

In Fig. 8, the electronic band structures of monolayer $GaInSe_3$ and $GaInTe_3$ with PBE and HSE06 are depicted, respectively. The band structures show an indirect bandgap nature using PBE and HSE06 potentials. The conduction band minimum (CBM) lies at the Γ point, and the valence band maximum (VBM) is on the Γ–M-path. The obtained bandgaps are in agreement with the results of the available literature.[38] The impact of Spin–Orbit Coupling (SOC) on the band structure was explored, considering the presence of heavy Se/Te atoms. Table IV summarizes the bandgap values calculated for the two monolayers using different potentials. The band edge shapes near the CBM and VBM changed substantially with the introduction of SOC. With the incorporation of SOC, both materials exhibit a direct bandgap semiconductor nature, with the VBM and CBM occurring at the Γ point in the Brillouin zone. A similar transition from indirect to direct bandgap by including SOC has been observed by Marfoua *et al.* for 2D $GaSe_{0.5}Te_{0.5}$ monolayers.[55] Furthermore, it was observed that the introduction of SOC led to a reduction in the bandgap for both $GaInSe_3$ and $GaInTe_3$ monolayers [shown in Fig. 9]. The calculated

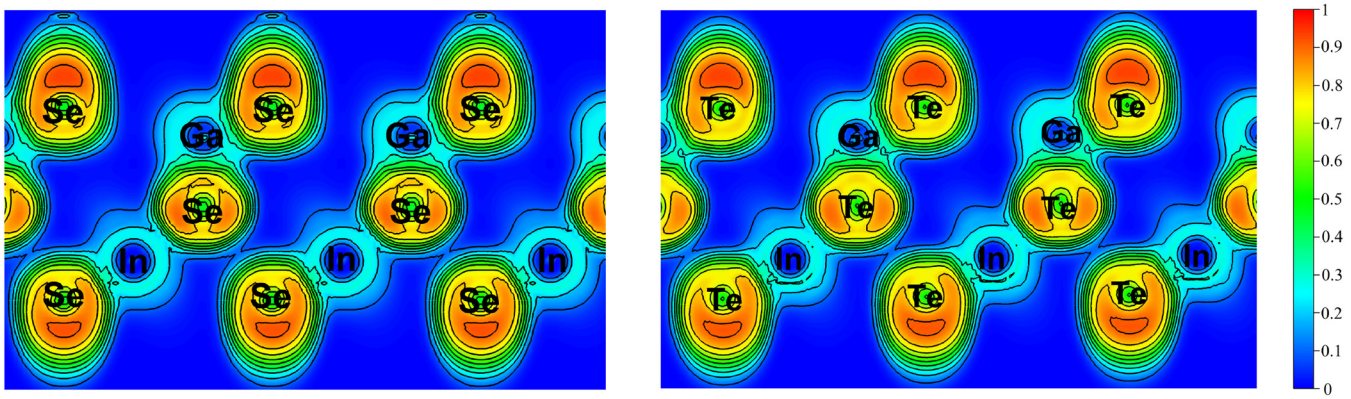

FIG. 7. Electron localization function plot of $GaInSe_3$ (left) and $GaInTe_3$ (right) for the (110) plain. The plots depict the variation in bonding for the central Te atom in $GaInTe_3$.

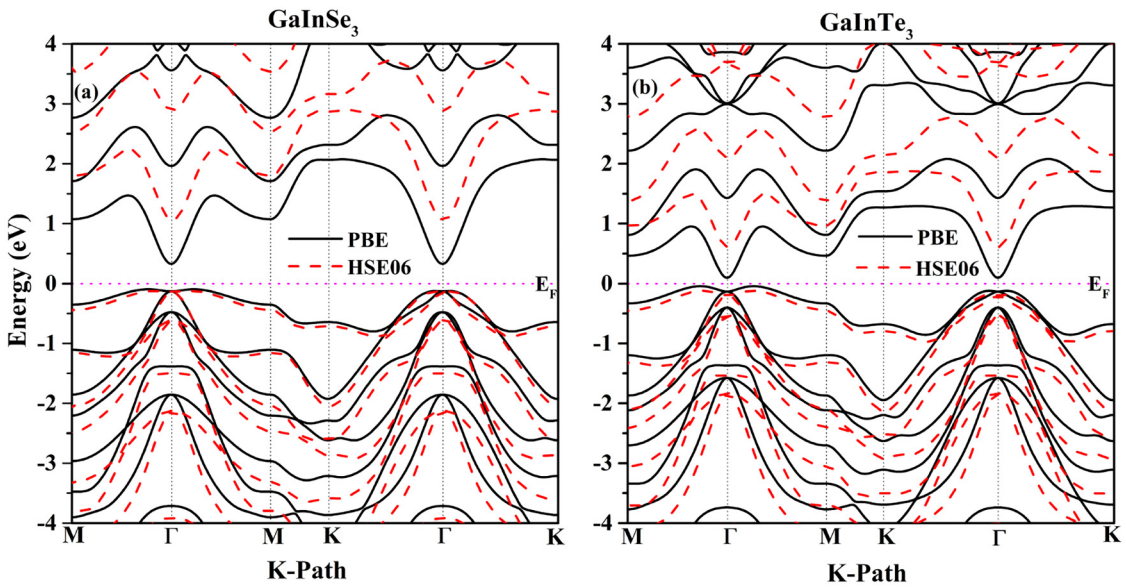

FIG. 8. Energy band diagrams of the $GaInSe_3$(a) and $GaInTe_3$(b) monolayers with PBE and HSE06 potentials.

bandgaps, determined using PBE + SOC, are reported as 0.3494 and 0.0417 eV for monolayers $GaInSe_3$ and $GaInTe_3$, respectively. However, it's noted that these values are underestimated compared to the results obtained with the HSE06 potential. The calculated bandgaps, determined using HSE + SOC, are reported as 1.0335 and 0.5318 eV for monolayers $GaInSe_3$ and $GaInTe_3$, respectively. In addition, spin–orbit coupling also splits the degenerate bands located at the Γ-point. The magnitude of the spin–orbit splitting of VBM at Γ-point is reported in Table V. It has been observed that the magnitude of spin–orbit splitting value increases as we go from Se to Te.

Understanding the electronic states near the Fermi level is crucial for evaluating transport properties. To this end, atomic projected density of state (PDOS) calculations were conducted. In $GaInSe_3$, the VBM primarily arises from Se-*p* orbitals, as well as from In-*p* and Ga-*p* states, while the CBM is chiefly contributed by the *p*-orbitals of Ga, In, and Se atoms [as depicted in Fig. 10(a)]. Similarly, in $GaInTe_3$, the VBM is predominantly influenced by Te-*p* orbitals, while the CBM is contributed by the *p*-orbitals of Ga, In, and Te atoms [as illustrated in Fig. 10(b)]. This observation suggests a significant degree of covalency in the electronic structure of both materials, despite the predominant presence of chalcogen states in the valence bands.

TABLE IV. Bandgap calculated for the monolayers $GaInSe_3$ and $GaInTe_3$ using different potentials.

Potential	$GaInSe_3$ (eV)	$GaInTe_3$ (eV)
PBE	0.4429	0.1729
	0.47[38]	0.25[38]
PBE + SOC	0.3494	0.0417
HSE06	1.1937	0.7449
	1.20[38]	0.75[38]
HSE06 + SOC	1.0335	0.5318

The effective mass of charge carriers is considered a key parameter in designing higher-efficiency TE materials as it plays a decisive role in affecting the carrier mobilities. The effective mass can be calculated using the parabolic band approximation with an energy dispersion relation

$$m^* = \hbar^2 / \left(\frac{\partial^2 E}{\partial k^2} \right).$$

Here, E and k are the energy and wave vector of the conduction band minimum (CBM) and valence band maximum (VBM). According to this definition, the effective mass of holes and electrons within the material exhibits an inverse relationship with the curvature of the bands in the electronic band structure. Specifically, a flatband corresponds to a lower effective mass. Table VI reports the effective mass values of charge carriers in the $GaInSe_3$ and $GaInTe_3$ monolayers. It is observed that the $GaInTe_3$ monolayer exhibits lower effective masses for both electrons and holes compared to the $GaInSe_3$ monolayer, indicating potentially favorable characteristics for higher carrier mobilities.

To calculate the electrical conductivity (σ), the relaxation time (τ) is essential, as the output in the BoltzTraP2 code is given by $\left(\frac{\sigma}{\tau}\right)$. A major challenge in predicting thermoelectric efficiency lies in calculating the relaxation time (τ). Various electron–phonon scattering mechanisms play a significant role at different temperatures in determining (τ). Acoustic phonon scattering is considered the primary scattering mechanism in thermoelectric materials. It is

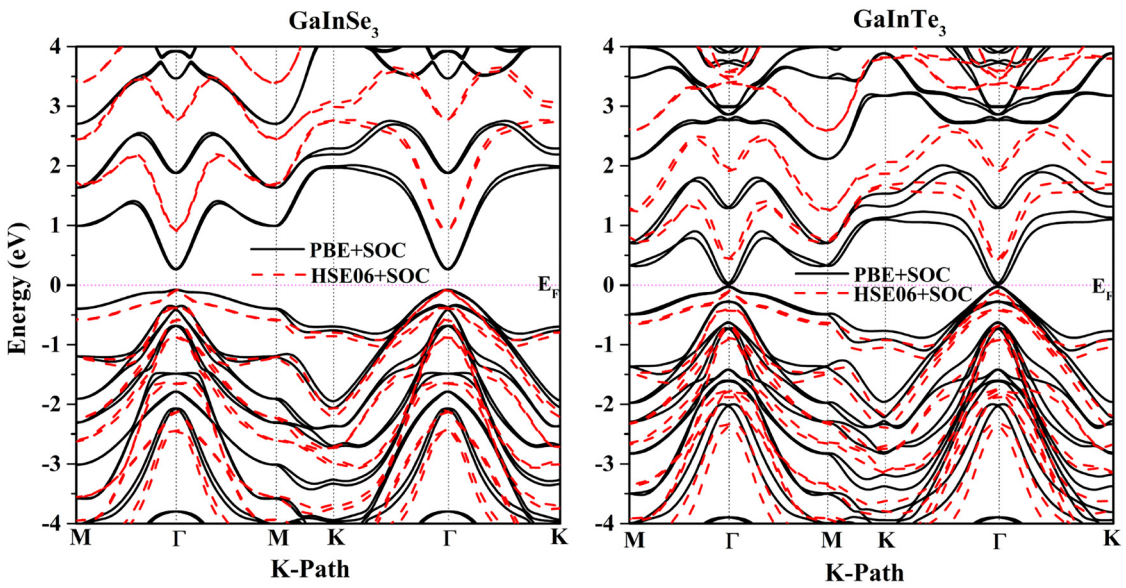

FIG. 9. Energy band diagrams of the $GaInSe_3$ and $GaInTe_3$ monolayers with PBE and HSE06 potentials including the effect of SOC.

evaluated by investigating carrier mobility based on the Bardeen–Shockley deformation potential (DP) theory. Herein, τ is determined by[47]

$$\tau = \frac{\mu_{2D} m^*}{e},$$

where μ_{2D} is carrier mobility, e is the electron charge, and m^* is the effective mass. In the deformation potential theory, the carrier mobility in 2D materials can be calculated by

$$\mu_{2D} = \frac{e\hbar^3 C}{k_B T m^* m_d E_1^2}.$$

Here, C represents the elastic modulus and can be calculated by

$$C = \frac{1}{A}\frac{\partial^2 E}{\partial \delta^2},$$

where E, δ, and A are the total energy, the applied strain, and the area at equilibrium for the 2D system, respectively. E_1 is deformation potential constant, defined as

$$E_1 = \frac{\Delta E_{\text{edge}}}{\Delta \delta},$$

where ΔE_{edge} is the energy change of band edges. m_d is average effective mass derived from $\sqrt{m_x^* m_y^*}$. The variation of band edge level with strain is plotted in Fig. S2 in the supplementary material.

It is important to note that in the deformation potential approximation, the dominant scattering process arises from the longitudinal acoustic phonon in the long-wavelength limit. Figure 11 shows the variation of mobility with temperature for $GaInSe_3$ and $GaInTe_3$. The mobility for $GaInTe_3$ was higher than $GaInSe_3$ for both types of charge carriers, i.e., holes and electrons. The difference in the value of mobility for holes is larger due to substantial difference in effective mass holes in the two compounds, as reported in Table VI. The mobility for both holes and electrons decreases with temperature, owing to an increased scattering of charge carriers.

Figure 12 shows the variation of relaxation time with temperature for the two compounds $GaInSe_3$ and $GaInTe_3$ for both holes and electrons. The relaxation time for electrons is larger than for holes in both materials. This is a consequence of the larger deformation potential constant and smaller effective mass of electrons.

The thermoelectric transport parameters can be calculated based on the relaxation time of charge carriers. The Seebeck coefficient and electrical conductivity show a strong dependence on the carrier concentration. Therefore, the TE parameters were calculated as a function of the charge carrier concentration at three temperatures (300, 500, 700 K). The obtained results are shown in the supplementary (Fig. S3 in the supplementary material). $|S|$ decreases

TABLE V. Spin–orbit splitting for the two monolayers at Γ-point.

	Spin–orbit splitting of bands at Γ-point (eV)	
Structure	PBE + SOC (eV)	HSE06 + SOC (eV)
$GaInSe_3$	0.249	0.312
$GaInTe_3$	0.253	0.318

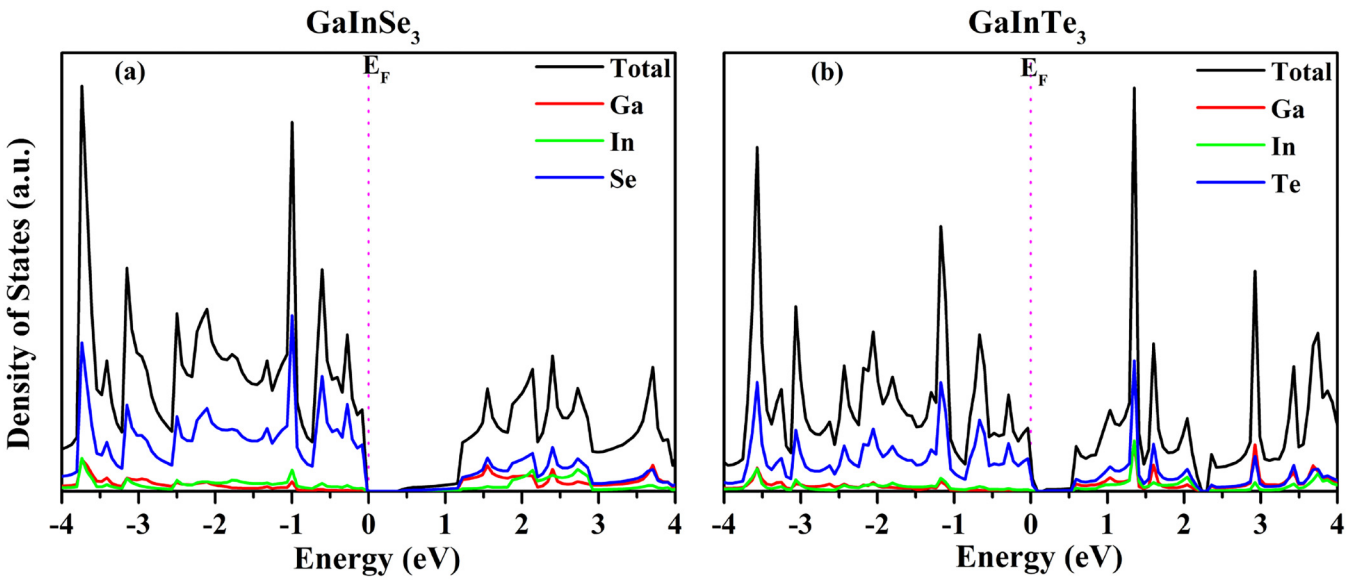

FIG. 10. Atom projected density of states of $GaInSe_3$ and $GaInTe_3$ monolayers.

with the carrier concentration, whereas σ increases with carrier concentration. The power factor (*PF*), given by $PF = S^2\sigma$, depends on S and σ. It quantifies the ability of a material to generate useful electrical power. In Fig. S2 in the supplementary material, the *PF* of both P-type and N-type increases with carrier concentration up to a peak value and then decreases. Due to the inverse relationship between S and σ, the maximum *PF* was obtained at the intermediate carrier concentration. The carrier concentration at which the *PF* was maximum was used to calculate the TE properties as a function of temperature for each monolayer.

Figure 13 depicts the variation of the Seebeck coefficient as a function of temperature for both $GaInSe_3$ and $GaInTe_3$ monolayers. The $|S|$ increased with increasing temperature. As expected, a positive Seebeck coefficient was observed for P-type doping, while a negative Seebeck coefficient was observed for N-type doping. The calculated Seebeck coefficient of $GaInSe_3$ and $GaInTe_3$ is 195 and $159\mu V\,K^{-1}$ for P-type doping and -137, and $-48\,\mu V\,K^{-1}$ for N-type doping at 300 K, respectively. The higher value of $|S|$ coefficient for $GaInSe_3$ is due to the larger effective mass of the charge carriers in $GaInSe_3$. Since the Seebeck coefficient is related to the effective mass of the charge carriers, which is given by the formula $S = \frac{8\pi^2 k_B^2}{3eh^2} m^* \left(\frac{\pi}{3n}\right)^{2/3} T$,[56] where n is the charge carrier concentration.

TABLE VI. The effective mass values for electrons and holes in $GaInSe_3$ and $GaInTe_3$ monolayers.

Charge carrier	$GaInSe_3$	$GaInTe_3$
Electron	$0.151\ m_e$	$0.116\ m_e$
Hole	$1.994\ m_e$	$0.523\ m_e$

Figure 14 shows the variation of the electrical conductivity of the $GaInSe_3$ and $GaInTe_3$ monolayer with temperature for P- and N-Type doping. The electrical conductivity decreases with increasing temperature as the charge carrier scattering increases. The electrical conductivity of $GaInTe_3$ was higher for both P- and N-type doping, as the electrical conductivity is inversely related to the effective mass of the charge carriers ($\sigma = ne\mu$).

The electronic thermal conductivity (κ_E) is expressed as $\kappa_E = L\sigma T$, according to Wiedmann–Franz's law, where L is the Lorenz factor. Generally, the constant L leads to higher value of electronic thermal conductivity and, thus, is a conservative estimation for the analysis of the zT value. As the Lorenz number is subject to variation across diverse materials, distinct carrier concentrations, and varying temperatures, a more precise Lorenz number is obtained through the formula $L = 1.5 + \exp\left[-\frac{|S|}{116}\right]$, where L is in $10^{-8}\,W\,\Omega\,K^{-2}$ and S in $\mu V/K$. Figure 15. shows the variation of the total thermal conductivity, which results from the sum of lattice thermal conductivity and electronic thermal conductivity. The value of the total thermal conductivity is higher with N-type doping than with P-type doping, as the electrical conductivity was higher with N-type doping.

The thermoelectric figure of merit for the monolayers $GaInSe_3$ and $GaInTe_3$ was calculated over a wide range of temperature by combining the Seebeck coefficient with the electrical and thermal conductivities [Fig. 16]. The zT value increases with temperature, which is attributed to the decrease in lattice thermal conductivity and the rise in the Seebeck coefficient. The zT value shows that $GaInTe_3$ performs better than $GaInSe_3$ for P-type doping, while $GaInSe_3$ performs better for N-type doping. This phenomenon was observed due to the increased electrical conductivity in the $GaInTe_3$ monolayer upon N-type doping, which increases the total

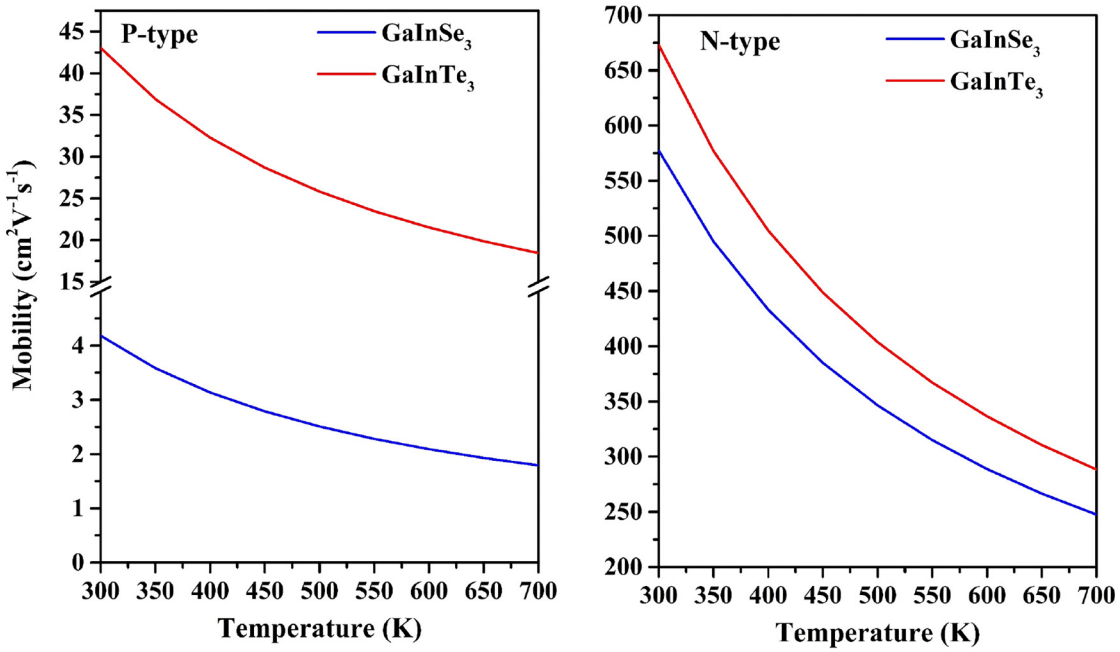

FIG. 11. Mobility obtained from DP theory as the function of temperature for holes (left) and electrons (right).

thermal conductivity in N-type doping and thus decreases the overall zT. The zT value in the case of $GaInSe_3$ P-type and N-type doping spans from 0.11 to 0.42 and 0.16 to 0.73 in the temperature range of 300 to 700 K, respectively, whereas in $GaInTe_3$ P-type and N-type doping, it spans from 0.65 to 2 and 0.08 to 0.46 in the temperature range from 300 to 700 K, respectively.

However, it is worth considering that the DP theory does not take into account the anharmonicity of phonons, especially the

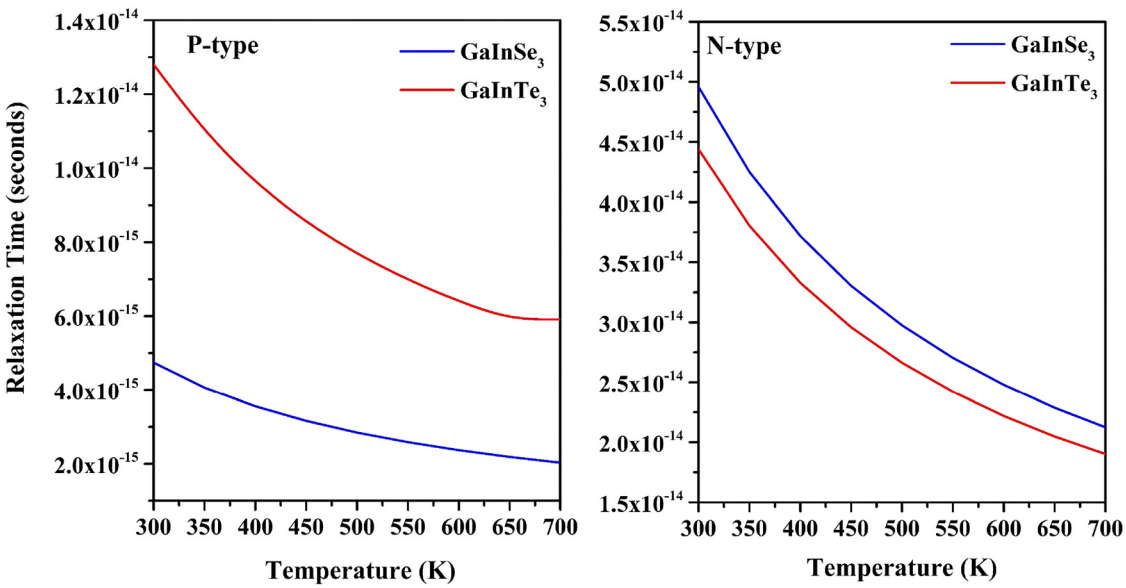

FIG. 12. Shows the resulting relaxation time of charge carriers as the function of temperature for holes (left) and electrons (right).

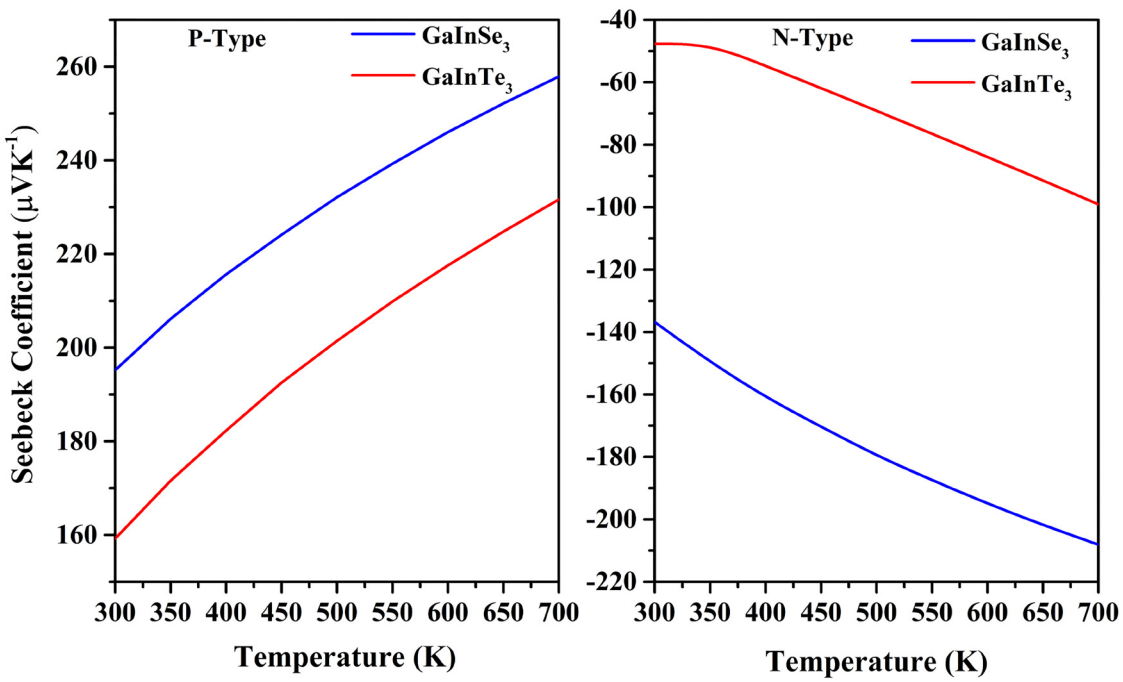

FIG. 13. The Seebeck coefficient for P- and N-type doping in $GaInSe_3$ and $GaInTe_3$ monolayers calculated in a temperature range from 300 to 700 K.

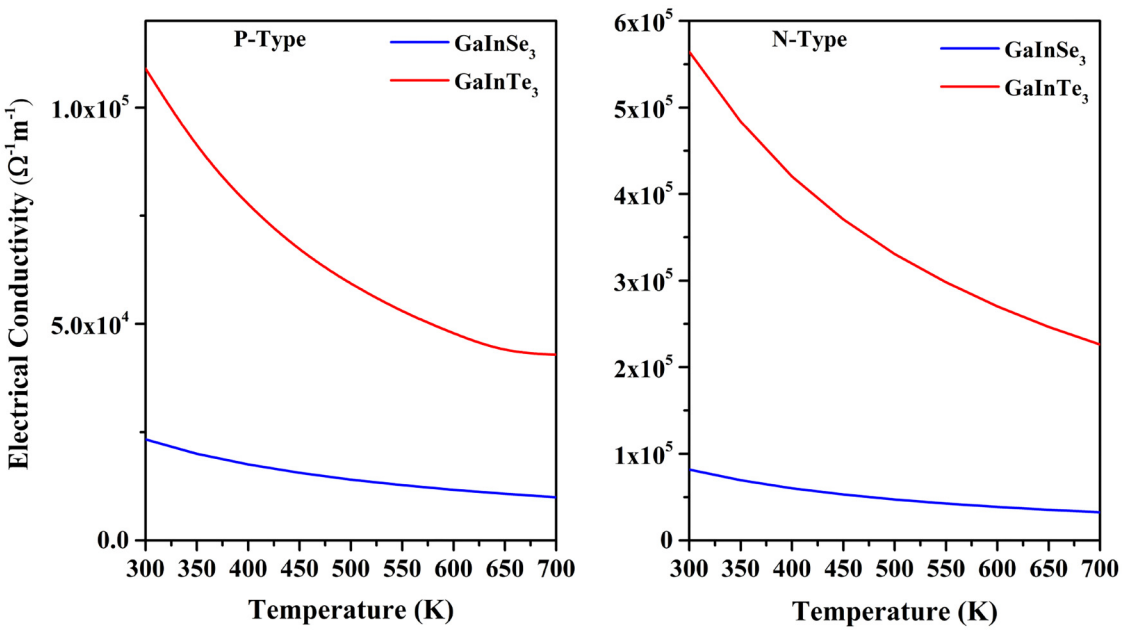

FIG. 14. The electrical conductivity for P-and N-type doping in $GaInSe_3$ and $GaInTe_3$ calculated in a temperature range from 300 to 700 K.

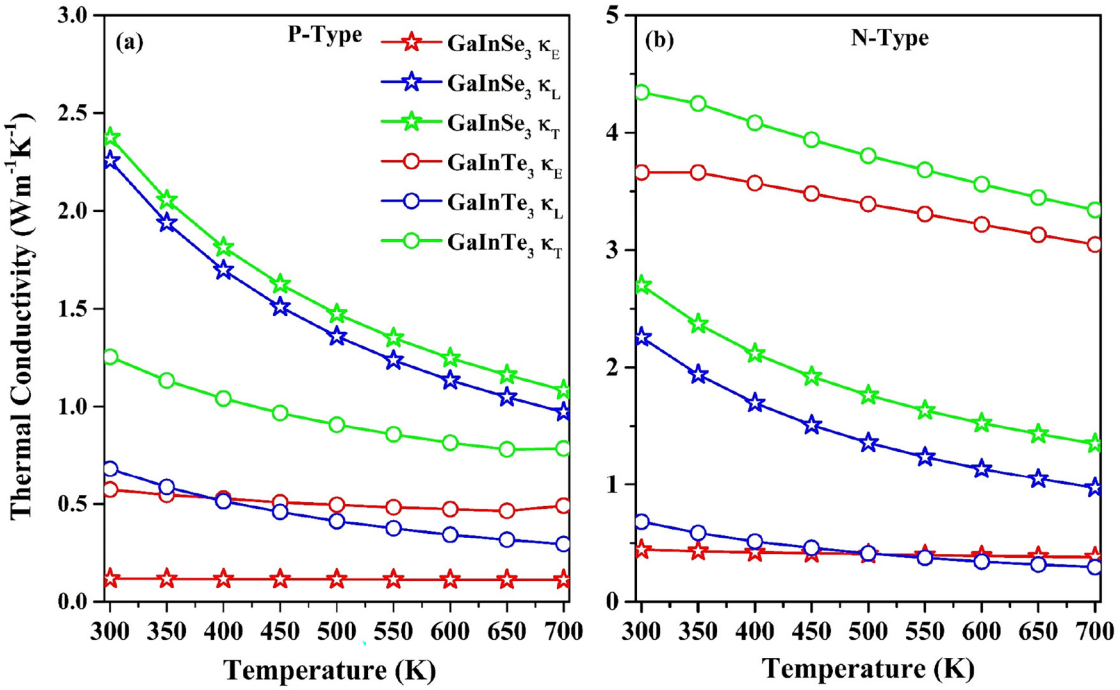

FIG. 15. The electronic, lattice, and total thermal conductivity of both P- and N-type doped $GaInSe_3$ and $GaInTe_3$. The calculations cover a temperature range spanning from 300 to 700 K.

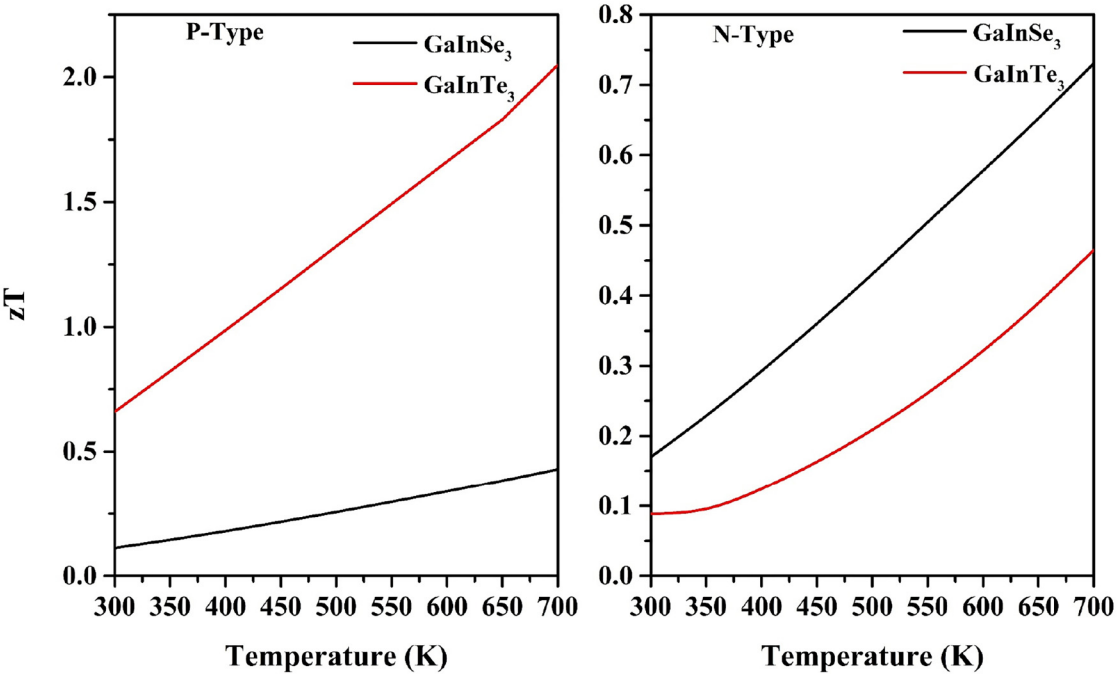

FIG. 16. The TE figure of merit for P-and N-type doping in $GaInSe_3$ and $GaInTe_3$ calculated in a temperature range from 300 to 700 K.

scattering between different phonons. As the temperature increases, the anharmonicity of phonons becomes more pronounced. Consequently, at high temperatures, scattering between phonons and charge carriers is weakened due to the strong phonon–phonon interactions. This can lead to an overestimation of the relaxation time and zT value of single-layer $GaInSe_3$ and $GaInTe_3$. In spite of these limitations, The DP theory is still widely used to approximate the relaxation time of 2D materials because the electron−phonon coupling method developed in recent years to calculate the electron relaxation time is extremely time-consuming.

IV. CONCLUSION

In summary, we have studied the thermal and thermoelectric transport properties of monolayer $GaInSe_3$ and $GaInTe_3$ via first-principles calculations combined with Boltzmann transport theory. Band structures show that both monolayers $GaInSe_3$ and $GaInTe_3$ are direct gap semiconductors with a bandgap of 1.0335 and 0.5318 eV using HSE06 + SOC potential, respectively. The lattice thermal conductivity is low, especially for $GaInTe_3$, which has a softer bonding than $GaInSe_3$. The calculated lattice thermal conductivity is 2.25 and 0.65 $W\,m^{-1}\,K^{-1}$ at room temperature for $GaInSe_3$ and $GaInTe_3$, respectively. Hence, the peak zT values of $GaInSe_3$ and $GaInTe_3$ at 700 K for the P-type doping reach to 0.5 and 2, respectively. While these values may be reduced due to other scattering mechanisms, they indicate that $GaInSe_3$ and $GaInTe_3$ monolayers have good potential for TE applications.

SUPPLEMENTARY MATERIAL

AIMD simulations showing the fluctuations of energy as a function of time step, Strain dependent band edge level and variation of thermoelectric transport parameters with the carrier concentration for both P- and N-type doping in $GaInSe_3$ and $GaInTe_3$ monolayers.

ACKNOWLEDGMENTS

The authors would like to acknowledge the support of the Italian Ministry of Universities and Research (MUR), in the framework of the project DICAM-EXC (Departments of Excellence 2023–2027, Grant No. L232/2016).

AUTHOR DECLARATIONS

Conflicts of Interest

The authors have no conflicts to disclose.

Author Contributions

Himanshu Nautiyal: Conceptualization (lead); Data curation (lead); Formal analysis (lead); Investigation (lead); Methodology (lead); Software (lead); Validation (equal); Visualization (equal); Writing – original draft (lead); Writing – review & editing (equal). **Paolo Scardi:** Conceptualization (equal); Funding acquisition (equal); Investigation (equal); Project administration (equal); Resources (equal); Software (equal); Supervision (equal); Validation (equal); Writing – review & editing (equal).

DATA AVAILABILITY

The data that support the findings of this study are available from corresponding authors upon reasonable request.

REFERENCES

[1]G. J. Snyder and E. S. Toberer, "Complex thermoelectric materials," Nat. Mater. 7(2), 105–114 (2008).
[2]J. Mao, Z. Liu, J. Zhou, H. Zhu, Q. Zhang, G. Chen, and Z. Ren, "Advances in thermoelectrics," Adv. Phys. **67**(2), 69–147 (2018).
[3]J. J. Gutiérrez Moreno, J. Cao, M. Fronzi, and M. H. N. Assadi, "A review of recent progress in thermoelectric materials through computational methods," Mater.: Renew. Sustain. Energy **9**(3), 1–22 (2020).
[4]Y. Xiao and L. D. Zhao, "Charge and phonon transport in PbTe-based thermoelectric materials," Npj Quantum Mater. **3**(1), 55 (2018).
[5]T. Cao, X. L. Shi, M. Li, B. Hu, W. Chen, W. Di Liu, W. Lyu, J. MacLeod, and Z. G. Chen, "Advances in bismuth-telluride-based thermoelectric devices: Progress and challenges," EScience **3**(3), 100122 (2023).
[6]M. S. Dresselhaus, G. Chen, M. Y. Tang, R. G. Yang, H. Lee, D. Z. Wang, Z. F. Ren, J. P. Fleurial, and P. Gogna, "New directions for low-dimensional thermoelectric materials," Adv. Mater. **19**(8), 1043–1053 (2007).
[7]J. P. Heremans, M. S. Dresselhaus, L. E. Bell, and D. T. Morelli, "When thermoelectrics reached the nanoscale," Nat. Nanotechnol. **8**(7), 471–473 (2013).
[8]N. M. R. Peres, "Colloquium: The transport properties of graphene: An introduction," Rev. Mod. Phys. **82**(3), 2673–2700 (2010).
[9]K. S. Novoselov, A. K. Geim, S. V. Morozov, D. Jiang, Y. Zhang, S. V. Dubonos, I. V. Grigorieva, and A. A. Firsov, "Electric field effect in atomically thin carbon films," Science **306**(5696), 666–669 (2016).
[10]S. Z. Butler, S. M. Hollen, L. Cao, Y. Cui, J. A. Gupta, H. R. Gutiérrez, T. F. Heinz, S. S. Hong, J. Huang, A. F. Ismach, E. Johnston-Halperin, M. Kuno, V. V. Plashnitsa, R. D. Robinson, R. S. Ruoff, S. Salahuddin, J. Shan, L. Shi, M. G. Spencer, M. Terrones, W. Windl, and J. E. Goldberger, "Progress, challenges, and opportunities in two-dimensional materials beyond graphene," ACS Nano **7**(4), 2898–2926 (2013).
[11]J. Sone, T. Yamagami, Y. Aoki, K. Nakatsuji, and H. Hirayama, "Epitaxial growth of silicene on ultra-thin Ag(111) films," New J. Phys. **16**(9), 095004 (2014).
[12]M. Derivaz, D. Dentel, R. Stephan, M. C. Hanf, A. Mehdaoui, P. Sonnet, and C. Pirri, "Continuous germanene layer on Al(111)," Nano Lett. **15**(4), 2510–2516 (2015).
[13]L. Li, Y. Yu, G. J. Ye, Q. Ge, X. Ou, H. Wu, D. Feng, X. H. Chen, and Y. Zhang, "Black phosphorus field-effect transistors," Nat. Nanotechnol. **9**(5), 372–377 (2014).
[14]Y. H. Chang, W. Zhang, Y. Zhu, Y. Han, J. Pu, J. K. Chang, W. T. Hsu, J. K. Huang, C. L. Hsu, M. H. Chiu, T. Takenobu, H. Li, C. I. Wu, W. H. Chang, A. T. S. Wee, and L. J. Li, "Monolayer MoSe2 grown by chemical vapor deposition for fast photodetection," ACS Nano **8**(8), 8582–8590 (2014).
[15]X. Wan, E. Z. Chen, J. Yao, M. Gao, X. Miao, S. Wang, Y. Gu, S. Xiao, R. Zhan, K. Chen, Z. Chen, X. Zeng, X. Gu, and J. Xu, "Synthesis and characterization of metallic Janus MoSH monolayer," ACS Nano **15**(12), 20319–20331 (2021).
[16]K. Zhang, Y. Guo, Q. Ji, A. Y. Lu, C. Su, H. Wang, A. A. Puretzky, D. B. Geohegan, X. Qian, S. Fang, E. Kaxiras, J. Kong, and S. Huang, "Enhancement of van der Waals interlayer coupling through polar Janus MoSSe," J. Am. Chem. Soc. **142**(41), 17499–17507 (2020).
[17]R. Sant, M. Gay, A. Marty, S. Lisi, R. Harrabi, C. Vergnaud, M. T. Dau, X. Weng, J. Coraux, N. Gauthier, O. Renault, G. Renaud, and M. Jamet, "Synthesis of epitaxial monolayer Janus SPtSe," Npj 2D Mater. Appl. **4**(1), 1–8 (2020).
[18]S. B. Harris, Y. C. Lin, A. A. Puretzky, L. Liang, O. Dyck, T. Berlijn, G. Eres, C. M. Rouleau, K. Xiao, and D. B. Geohegan, "Real-Time diagnostics of 2D crystal transformations by pulsed laser deposition: Controlled synthesis of Janus WSSe monolayers and alloys," ACS Nano **17**(3), 2472–2486 (2023).

[19]B. Liu, J. Liu, G. Miao, S. Xue, S. Zhang, L. Liu, X. Huang, X. Zhu, S. Meng, J. Guo, M. Liu, and W. Wang, "Flat AgTe honeycomb monolayer on Ag(111)," J. Phys. Chem. Lett. **10**(8), 1866–1871 (2019).
[20]K. Chang and S. S. P. Parkin, "Experimental formation of monolayer group-IV monochalcogenides," J. Appl. Phys. **127**(22), 220902 (2020).
[21]Q. H. Wang, K. Kalantar-Zadeh, A. Kis, J. N. Coleman, and M. S. Strano, "Electronics and optoelectronics of two-dimensional transition metal dichalcogenides," Nat. Nanotechnol. **7**(11), 699–712 (2012).
[22]K. F. Mak and J. Shan, "Photonics and optoelectronics of 2D semiconductor transition metal dichalcogenides," Nat.: Photonics **10**(4), 216–226 (2016).
[23]D. Li, Y. Gong, Y. Chen, J. Lin, Q. Khan, Y. Zhang, Y. Li, H. Zhang, and H. Xie, "Recent Progress of Two-Dimensional Thermoelectric Materials," Nano-Micro Lett. **12**(1), 36 (2020).
[24]J. Z. Ou, W. Ge, B. Carey, T. Daeneke, A. Rotbart, W. Shan, Y. Wang, Z. Fu, A. F. Chrimes, W. Wlodarski, S. P. Russo, Y. X. Li, and K. Kalantar-Zadeh, "Physisorption-based charge transfer in two-dimensional SnS_2 for selective and reversible NO_2 gas sensing," ACS Nano **9**(10), 10313–10323 (2015).
[25]Y. Sun, H. Cheng, S. Gao, Z. Sun, Q. Liu, Q. Leu, F. Lei, T. Yao, J. He, S. Wei, and Y. Xie, "Freestanding tin disulfide single-layers realizing efficient visible-light water splitting," Angew. Chem. Int. Ed. **51**(35), 8727–8731 (2012).
[26]C. Cui, F. Xue, W. J. Hu, and L. J. Li, "Two-dimensional materials with piezoelectric and ferroelectric functionalities," Npj 2D Mater. Appl. **2**(1), 18 (2018).
[27]A. Kandemir and H. Sahin, "Janus single layers of In_2SSe: A first-principles study," Phys. Rev. B **97**(15), 1–7 (2018).
[28]A. Y. Lu, H. Zhu, J. Xiao, C. P. Chuu, Y. Han, M. H. Chiu, C. C. Cheng, C. W. Yang, K. H. Wei, Y. Yang, Y. Wang, D. Sokaras, D. Nordlund, P. Yang, D. A. Muller, M. Y. Chou, X. Zhang, and L. J. Li, "Janus monolayers of transition metal dichalcogenides," Nat. Nanotechnol. **12**(8), 744–749 (2017).
[29]A. Kandemir and H. Sahin, "Bilayers of Janus WSSe: Monitoring the stacking type via the vibrational spectrum," Phys. Chem. Chem. Phys. **20**(25), 17380–17386 (2018).
[30]A. Patel, D. Singh, Y. Sonvane, P. B. Thakor, and R. Ahuja, "High thermoelectric performance in Two-dimensional Janus monolayer material WS-X (X = Se and Te)," ACS Appl. Mater. Interfaces **12**(41), 46212–46219 (2020).
[31]S. D. Guo, X. S. Guo, R. Y. Han, and Y. Deng, "Predicted Janus SnSSe monolayer: A comprehensive first-principles study," Phys. Chem. Chem. Phys. **21**(44), 24620–24628 (2019).
[32]H. Nautiyal and P. Scardi, "First principles study of SnX_2 (X = S, Se) and Janus SnSSe monolayer for thermoelectric applications," Nanotechnology **33**(32), 325402 (2022).
[33]T. V. Vu, V. T. T. Vi, H. V. Phuc, C. V. Nguyen, N. A. Poklonski, C. A. Duque, D. P. Rai, B. D. Hoi, and N. N. Hieu, "Electronic, optical, and thermoelectric properties of Janus In-based monochalcogenides," J. Phys. Condens. Matter **33**(22), 225503 (2021).
[34]G. Almeida, S. Dogan, G. Bertoni, C. Giannini, R. Gaspari, S. Perissinotto, R. Krahne, S. Ghosh, and L. Manna, "Colloidal monolayer β-In2Se3 nanosheets with high photoresponsivity," J. Am. Chem. Soc. **139**(8), 3005–3011 (2017).
[35]H. D. Bui, H. R. Jappor, and N. N. Hieu, "Tunable optical and electronic properties of Janus monolayers Ga2SSe, Ga2STe, and Ga2SeTe as promising candidates for ultraviolet photodetectors applications," Superlattices Microstruct. **125**(2018), 1–7 (2019).
[36]Q. Zhong, Z. Dai, J. Liu, Y. Zhao, and S. Meng, "Phonon thermal transport in Janus single layer M2XY (M = Ga; X, Y = S, Se, Te): A study based on first-principles," Phys. E **115**(2019), 113683 (2020).
[37]B. P. Bahuguna, L. K. Saini, R. O. Sharma, and B. Tiwari, "Hybrid functional calculations of electronic and thermoelectric properties of GaS, GaSe, and GaTe monolayers," Phys. Chem. Chem. Phys. **20**(45), 28575–28582 (2018).
[38]T. V. Vu, N. N. Hieu, A. A. Lavrentyev, O. Y. Khyzhun, C. V. Lanh, A. I. Kartamyshev, H. V. Phuc, and N. V. Hieu, "Novel Janus GaInX3 (X = S, Se, Te) single-layers: First-principles prediction on structural, electronic, and transport properties," RSC Adv. **12**(13), 7973–7979 (2022).
[39]G. Kresse and J. Furthmüller, "Efficient iterative schemes for *ab initio* total-energy calculations using a plane-wave basis set," Phys. Rev. B **54**(16), 11169–11186 (1996).
[40]G. Kresse and J. Furthmüller, "Efficiency of ab-initio total energy calculations for metals and semiconductors using a plane-wave basis set," Comput. Mater. Sci. **6**(1), 15–50 (1996).
[41]J. P. Perdew, K. Burke, and M. Ernzerhof, "Generalized gradient approximation made simple," Phys. Rev. Lett. **77**(18), 3865–3868 (1996).
[42]S. Grimme, J. Antony, S. Ehrlich, and H. Krieg, "A consistent and accurate *ab initio* parametrization of density functional dispersion correction (DFT-D) for the 94 elements H-Pu," J. Chem. Phys. **132**(15), 154104 (2010).
[43]H. J. Monkhorst and J. D. Pack, "Special points for brillouin-zone integrations," Phys. Rev. B **13**(12), 5188–5192 (1976).
[44]A. Togo and I. Tanaka, "First principles phonon calculations in materials science," Scr. Mater. **108**, 1–5 (2015).
[45]A. Togo, L. Chaput, and I. Tanaka, "Distributions of phonon lifetimes in Brillouin zones," Phys. Rev. B **91**(9), 094306 (2015).
[46]G. K. H. Madsen, J. Carrete, and M. J. Verstraete, "Boltztrap2, a program for interpolating band structures and calculating semi-classical transport coefficients," Comput. Phys. Commun. **231**, 140–145 (2018).
[47]J. Bardeen and W. Shockley, "Deformation potentials and mobilities in non-polar crystals," Phys. Rev. **80**(1), 72–80 (1950).
[48]K. Momma and F. Izumi, "VESTA: A three-dimensional visualization system for electronic and structural analysis," J. Appl. Crystallogr. **41**(3), 653–658 (2008).
[49]V. Wang, G. Tang, Y. C. Liu, R. T. Wang, H. Mizuseki, Y. Kawazoe, J. Nara, and W. T. Geng, "High-throughput computational screening of two-dimensional semiconductors," J. Phys. Chem. Lett. **13**(50), 11581–11594 (2022).
[50]O. L. Anderson, "A simplified method for calculating the Debye temperature from elastic constants," J. Phys. Chem. Solids **24**, 909–917 (1963).
[51]R. Hill, "The elastic behaviour of a crystalline aggregate," Proc. Phys. Soc. Sect. A **65**(5), 349–354 (1952).
[52]Y. Zhang, X. Ke, C. Chen, J. Yang, and P. R. C. Kent, "Thermodynamic properties of PbTe, PbSe, and PbS: First-principles study," Phys. Rev. B: Condens. Matter Mater. Phys. **80**(2), 1–12 (2009).
[53]F. Q. Wang, S. Zhang, J. Yu, and Q. Wang, "Thermoelectric properties of single-layered SnSe sheet," Nanoscale **7**(38), 15962–15970 (2015).
[54]E. S. Toberer, L. L. Baranowski, and C. Dames, "Advances in thermal conductivity," Annu. Rev. Mater. Res. **42**(1), 179–209 (2012).
[55]B. Marfoua and J. Hong, "Giant thermoelectric performance of an n-type 2D $GaSe_{0.5}Te_{0.5}$ alloy," J. Mater. Chem. C **9**(32), 10497–10504 (2021).
[56]J. P. Heremans, "Low-dimensional thermoelectricity," Acta Phys. Pol. A **108**(4 PART 1), 609–634 (2005).